STScI | SPACE TELESCOPE SCIENCE INSTITUTE

Instrument Science Report STIS 2022-06(v1)

Flux Repeatability of FUV-MAMA Spectra as a Function of Cross-dispersion Position

Leonardo A. Dos Santos[1]

[1] Space Telescope Science Institute, Baltimore, MD

30 September 2022

ABSTRACT

The data reduction of STIS raw spectra was originally designed to apply three different flat fields: pixel-to-pixel level corrections (P-flats), low-frequency corrections in scales of tens of pixels (L-flats), and time variability corrections (D-flats). However, in the case of FUV-MAMA, the L-flat reference file currently only corrects for vignetting of the G140L mode and no other low-frequency corrections are applied. In this document, we analyze calibration data obtained in Cycle 28 across the detector to test whether any uncorrected low spatial frequency variations exceed the accuracy specifications of the instrument. We find that the FUV-MAMA fluxes are mostly repeatable at different cross-dispersion positions in the detector, with the exception of G140M centered at 1567 Å. We also provide recommendations of when (or ever) users should request disabling monthly offsets, which is an available but unsupported mode starting in Cycle 30.

Contents

1. Introduction

The Space Telescope Imaging Spectrograph (STIS) is the most versatile instrument aboard the *Hubble Space Telescope* (*HST*), covering wavelengths from far-ultraviolet (FUV) to near infrared (NIR). A complete list of its capabilities is listed in Section 3.1 of the instrument handbook (Prichard, Welty & Jones 2022). STIS possesses three different detectors: the CCD, which is used for observations in the optical and NIR, and two Multi-Anode Microchannel Arrays (MAMAs) for FUV and near-ultraviolet (NUV) observations.

Since the STIS detectors are photon- or electron-counting devices, they do not directly measure the flux of astronomical sources. Instead, we need to convert the count-rates measured in the detectors into an absolute flux unit of [energy time^{-1} area^{-1}]. The accuracy of astronomical observations relies on how accurate the flux calibration is. In particular, STIS FUV fluxes are calibrated by matching observations of white dwarf flux standards with theoretical models of their spectra (see Bohlin, Collins & Gonnella 1998 for the low-resolution modes and Proffitt 2006 for the medium-resolution modes). Furthermore, the MAMAs suffer from wavelength-dependent degradation, leading to loss of sensitivity as time passes (Carlberg & Monroe 2017). This is the main motivation for efforts to track the time-dependent sensitivity (TDS) of these detectors and performing regular absolute flux calibrations.

The STIS instrument handbook (Prichard, Welty & Jones 2022) specifies that the absolute flux accuracy of the instrument is 4% for low-resolution (L) modes and 5% for medium-resolution (M) modes, valid for the photometric 2-arcsecond slit. These are considered typical accuracies, and they can vary by a factor of 2 or 3 depending on wavelength. Recent flux recalibration efforts of the STIS instrument show that intrinsic errors in the absolute flux calibration contribute to less than 1% in most wavelengths in the FUV, so the 4%-5% quoted above encompass other sources of errors (e.g., uncorrected detector non-uniformities, instrument stability, accuracy of the TDS). In this document, we aim to assess the contribution from uncorrected detector non-uniformites by evaluating the flux repeatability of a standard star in several cross-dispersion positions across the FUV-MAMA detector and the gratings G140L and G140M.

One of the main motivations for this investigation is trying to understand the larger scatter in the relative count rates after correcting for the TDS (i.e., the residual TDS). In the TDS monitor, three measurements in particular stood out as sitting well below the general TDS trend (Fig. 1), and two of these had systematically low A2CENTER values[1]. Furthermore, the lack of repeatability is often attributed to monthly offsets of STIS, which position the spectral traces in regions with potentially

[1] `A2CENTER` is the cross-dispersion location of the spectral trace at the dispersion position of 512 in

uncorrected detector non-uniformities. The monthly offsets are intentional shifts of up to ± 15 (± 40) low-resolution pixels in the dispersion (cross-dispersion) direction that have been used in 1st order spectroscopy since January 1998 to minimize uneven charge depletion in the microchannel plates, which could increase non-uniformity in flat fields. More information about the monthly offsets can be found in Section 7.6.2 of the instrument handbook (Prichard, Welty & Jones 2022). However, a recent analysis has not found any evidence that the MAMA detectors show uneven charge depletion thus far (Maclay 2021).

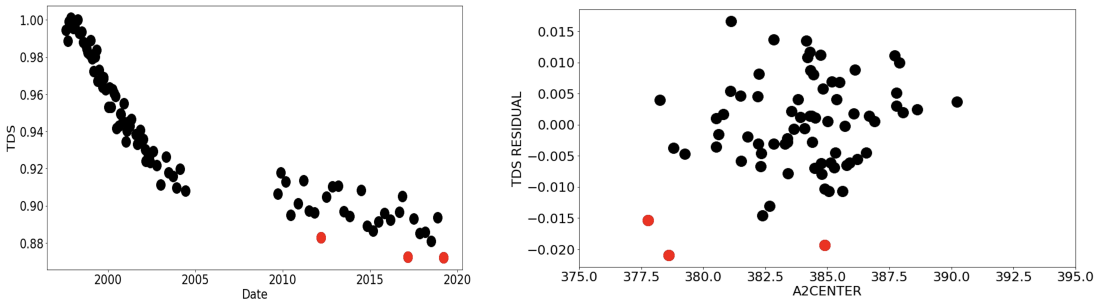

Figure 1. *Left panel*: Variation of the time-dependent sensitivity monitor (TDS) of STIS, with the three outlier points marked in red. *Right panel*: `A2CENTER` positions versus TDS residual plot, showing that two of the red outlier points are located at low values of `A2CENTER`.

For spectrophotometric measurements with the MAMA detectors, the main limiting factor in the measurement accuracy could be how well we can correct for detector non-uniformities. In this scenario, the floor that would set the photometric accuracy is the flat-fielding procedure. The original, on-orbit, flat-fielding strategy to correct for detector non-uniformities for STIS was discussed by Bohlin, Lindler & Baum (1996). Due to the high counts requirement to achieve a S/N of 100 per resolution element, the authors discuss the need to use indirect estimates of the flat field correction files to avoid long exposure times with the internal krypton (Kr) and deuterium (D_2) lamps. The STIS flat-fielding strategy was supposed to involve three calibration files: the pixel-to-pixel flat, P or PFLTFILE, which corrects for non-uniformities at high frequencies; the low-frequency flat, L or LFLTFILE; and the time-variable delta flat, D or DFLTFILE. However, the DFLTFILE was never implemented. Currently only the G140L grating has a true LFLTFILE among the FUV modes (see Fig. 2), while G140M and the echelle gratings (E140M and E140M) have dummy L-flats filled with `1.0` in all pixels. See more details about the P-flat strategy for STIS in Shaw, Kaiser & Ferguson (1998).

To assess the flat-fielding performance of the FUV-MAMA, we observed the standard white dwarfs GD 153 and G 191-B2B (respectively for the low- and medium-resolution modes) in the calibration program PID 16438 between February

low-resolution pixel space.

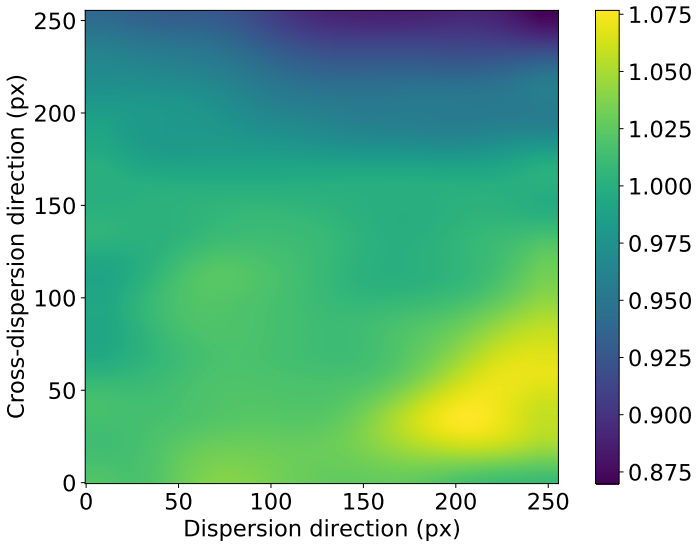

Figure 2. The L-flat that is currently applied to G140L observations. The grid is undersampled at 256x256 pixels to capture the lower-frequency variations.

2021 and October 2021. We used the G140L and G140M gratings coupled with the photometric aperture 52x2 arcsec, and varied the position of the target in the cross-dispersion direction. This offset was done by applying shifts in the axis 2 direction (POSTARG2) and are listed in Tables 1, 2 and 3 and can be seen in the stacked raw images in Fig. 3. The POSTARG2 parameter was varied in three sets of offsets: i) between -1.0 and 1.0 for the nominal position, ii) between -1.0 and 1.0 for the D1 position[2], and iii) between -3.2 and 13.5 around the nominal position to semi-regularly sample the remaining regions, avoiding the repeller wire at the detector center and the fiducial bar near the top. The observations and their logs are listed in Tables 1, 2 and 3. The raw data are shown in Fig. 3. The reason why the longer wavelength CENWAVE observations did not step across the slit is that they were added to double check for any potential wavelength dependence. Since the star is fainter at these longer wavelengths (and the observations more expensive) than the other 2 settings, it was decided that gathering observations around nominal and D1 was sufficient for the test.

Assuming that all differences between the observed spectra are due to detector non-uniformities, we assess how repeatable they are in context with the instrument's accuracy requirements. Additionally, we aim to determine whether effort should be spent on the creation of true L-flats for G140M, updating the L-flat for G140L, and provide recommendations of when users should disable monthly offsets to achieve their flux accuracy goals.

[2]The D1 position is a region of the FUV-MAMA detector with relatively low dark background contamination, which is ideal for observing faint targets. The trade-off is that this region is not as well characterized as the nominal position.

Table 1. Observations log of the calibration data for optical element G140L (central wavelength 1425 Å).

Dataset	Aperture	Exp. time (s)	Offset (arcsec)	Obs. date (UT)
oehp01010	52X2	245.0	-0.99	2021-02-14 09:32:55
oehp01020	52X2	245.0	-0.66	2021-02-14 09:39:21
oehp01030	52X2	245.0	-0.33	2021-02-14 09:44:14
oehp01040	52X2	245.0	0.0	2021-02-14 09:49:07
oehp01050	52X2	245.0	0.33	2021-02-14 09:54:00
oehp01060	52X2	245.0	0.66	2021-02-14 09:58:53
oehp01070	52X2	245.0	0.99	2021-02-14 10:03:46
oehp03010	52X2	244.0	-3.2	2021-03-26 10:43:21
oehp03020	52X2	244.0	-2.6	2021-03-26 10:49:46
oehp03030	52X2	244.0	5.1	2021-03-26 10:54:47
oehp03040	52X2	244.0	7.2	2021-03-26 10:59:41
oehp03050	52X2	244.0	9.3	2021-03-26 11:04:35
oehp03070	52X2	244.0	13.5	2021-03-26 11:14:23
oehp02010	52X2D1	245.0	-0.99	2021-02-14 11:08:22
oehp02020	52X2D1	245.0	-0.66	2021-02-14 11:14:48
oehp02030	52X2D1	245.0	-0.33	2021-02-14 11:19:41
oehp02040	52X2D1	245.0	0.0	2021-02-14 11:24:34
oehp02050	52X2D1	245.0	0.33	2021-02-14 11:29:27
oehp02060	52X2D1	245.0	0.66	2021-02-14 11:34:20
oehp02070	52X2D1	245.0	0.99	2021-02-14 11:39:13

Table 2. Same as Table 1, but for optical element G140M (central wavelength 1272 Å).

Dataset	Aperture	Exp. time (s)	Offset (arcsec)	Obs. date (UT)
oehp04010	52X2	243.0	-0.99	2021-08-27 12:14:13
oehp04020	52X2	243.0	-0.66	2021-08-27 12:20:39
oehp04030	52X2	243.0	-0.33	2021-08-27 12:25:32
oehp04040	52X2	243.0	0.0	2021-08-27 12:30:25
oehp04050	52X2	243.0	0.33	2021-08-27 12:35:18
oehp04060	52X2	243.0	0.66	2021-08-27 12:40:11
oehp04070	52X2	243.0	0.99	2021-08-27 12:45:04
oehp06010	52X2	241.0	-3.2	2021-09-03 02:59:36
oehp06020	52X2	241.0	-2.6	2021-09-03 03:06:00
oehp06030	52X2	241.0	5.1	2021-09-03 03:11:00
oehp06040	52X2	241.0	7.2	2021-09-03 03:15:53
oehp06050	52X2	241.0	9.3	2021-09-03 03:20:46
oehp06060	52X2	241.0	10.5	2021-09-03 03:25:37
oehp06070	52X2	241.0	13.5	2021-09-03 03:30:32
oehp05010	52X2D1	241.0	-0.99	2021-09-01 03:22:02
oehp05020	52X2D1	241.0	-0.66	2021-09-01 03:28:26
oehp05030	52X2D1	241.0	-0.33	2021-09-01 03:33:17
oehp05040	52X2D1	241.0	0.0	2021-09-01 03:38:08
oehp05050	52X2D1	241.0	0.33	2021-09-01 03:42:59
oehp05060	52X2D1	241.0	0.66	2021-09-01 03:47:50
oehp05070	52X2D1	241.0	0.99	2021-09-01 03:52:41

Table 3. Same as Table 1, but for optical element G140M (central wavelength 1567 Å).

Dataset	Aperture	Exp. time (s)	Offset (arcsec)	Obs. date (UT)
oehp07010	52X2	453.0	-1.0	2021-10-20 23:33:24
oehp07020	52X2	453.0	-0.67	2021-10-20 23:43:20
oehp07030	52X2	453.0	-0.33	2021-10-20 23:51:43
oehp07040	52X2	453.0	0.0	2021-10-21 00:00:06
oehp07050	52X2	453.0	0.33	2021-10-21 01:00:16
oehp07060	52X2	453.0	0.67	2021-10-21 01:08:39
oehp07070	52X2	453.0	1.0	2021-10-21 01:17:02
oehp07080	52X2D1	453.0	-1.0	2021-10-21 01:25:35
oehp07090	52X2D1	453.0	-0.67	2021-10-21 01:33:58
oehp070a0	52X2D1	453.0	-0.33	2021-10-21 02:35:31
oehp070b0	52X2D1	453.0	0.0	2021-10-21 02:43:54
oehp070c0	52X2D1	453.0	0.33	2021-10-21 02:52:17
oehp070d0	52X2D1	453.0	0.67	2021-10-21 03:00:40
oehp070e0	52X2D1	453.0	1.0	2021-10-21 03:09:03

2. Analysis of the calibration data

As an initial step, we took the pipeline-extracted `x1d` spectra at face value and calculated the ratios of the extracted spectra at different positions in the detector in relation to the nominal position. Upon the verification of some wavelength-dependent, low-frequency trends in the pipeline products, we attempted to refine the spectral extraction by applying custom traces, as these are the usual cause for wavelength-dependent errors in spectral extraction.

The pipeline spectra were originally extracted using spectral traces defined by the reference file `q8l14504o_1dt.fits`. Essentially, this reference file contains the traces previously calculated for fixed `A2CENTER` positions, which are then interpolated to the specific `A2CENTER` position used as input for the extraction procedure. To get around the pipeline traces, we fit empirical traces to the observed spectra of this program, modify the reference file and re-process the flat-fielded `flt` files using the custom reference file.

The empirical traces are calculated by fitting the observed spatial profiles with a double Gaussian containing a narrow and a wide component with a common center; to this end, we use the `optimize.minimize` method from SciPy (Virtanen et al. 2020). We fit a profile for each low-resolution element in the dispersion direction; the five free parameters of the fit are the center of the spatial profile and the width and amplitude of each Gaussian component. We show examples of two such fits in Fig. 4; the spatial profile of G140M spectra shows a more substantial contribution from the wide Gaussian component than the G140L spectra.

The center of the spatial profiles across the dispersion direction in the detector will define the empirical traces that we wish to measure. The measured centers have a scatter due to imperfect fits and photon noise from the measured count rates. We smooth them

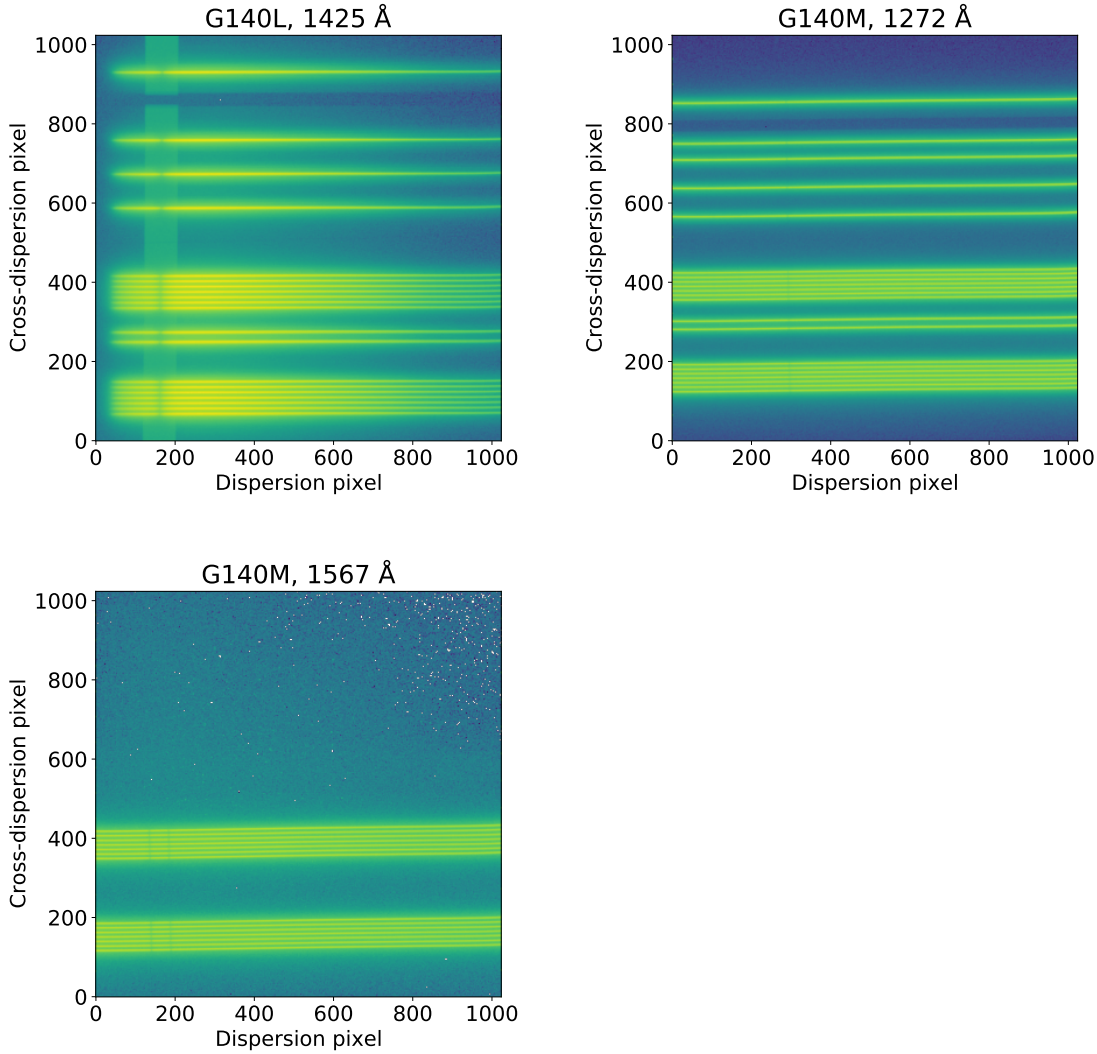

Figure 3. Superimposed exposures of the calibration data for the three different instrument configurations in the program. The D1 positions are located $\lesssim$ 200 px in the cross-dispersion direction.

out by fitting the measured centers as a function of cross-dispersion pixel using 6th- and 7th-order polynomials for G140M and G140L spectra, respectively. We show the differences between the custom traces and pipeline traces in Fig. 5. These differences vary between 0.25 and 0.50 pixels for the G140M mode, and up to 1.5 pixel for the G140L mode. They could partially be caused by a rotation of the traces (see Dressel et al. 2007) after the Servicing Mission 4 (SM4).

For the D1 positions, we omit the background removal. We found this was necessary because the extraction of D1 positions is optimized for faint spectra, for which the background is extracted from distances of only 30 pixels from the spectral trace (for

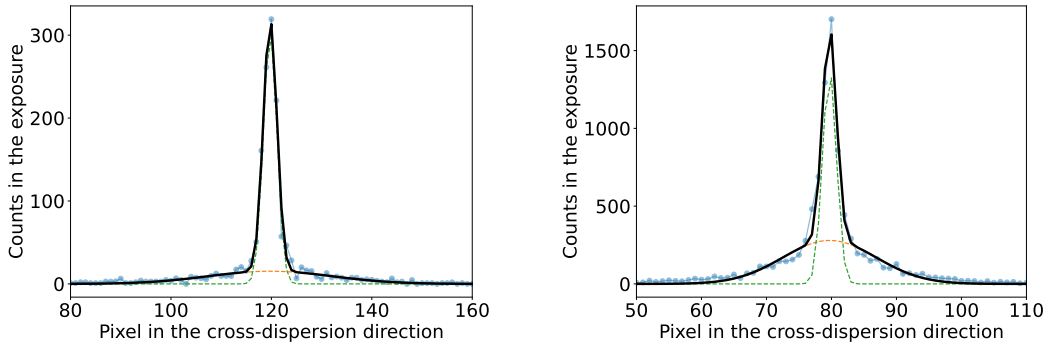

Figure 4. Examples of spatial profile fits for arbitrary spectral positions using the G140L (left) and G140M (right) gratings. The green profile represents the narrow Gaussian component, while the orange one stands for the wider component. The black profile is the combination of both narrow and wide components. The observed data is shown in blue.

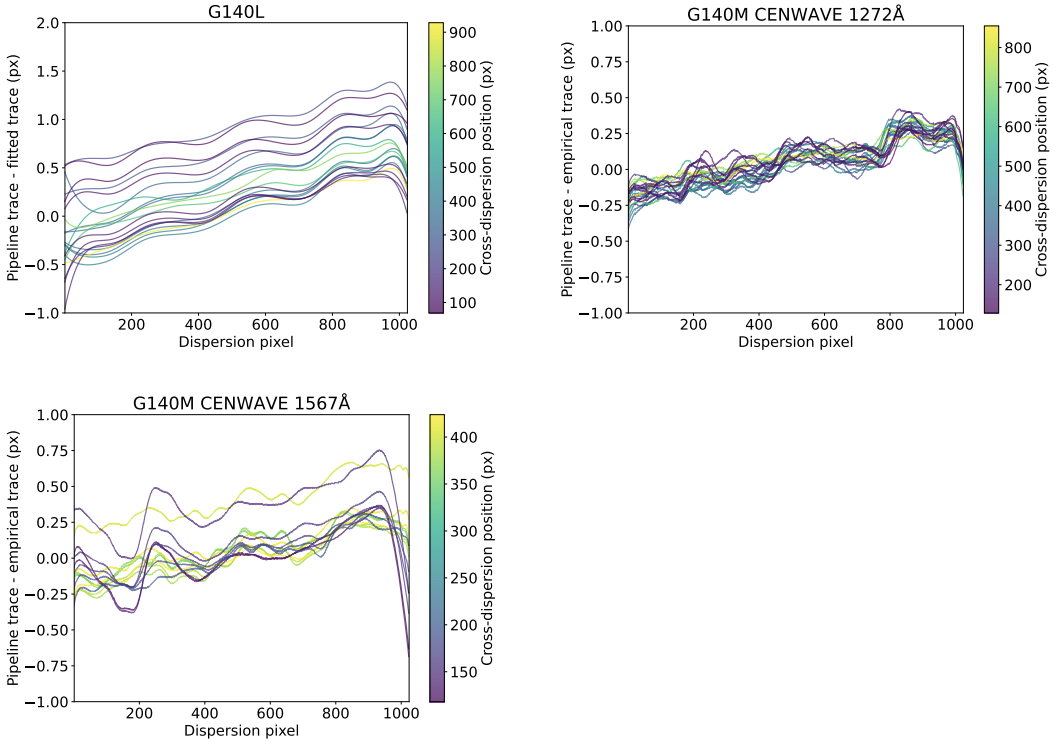

Figure 5. Differences between the empirical spectral traces we measured in the calibration data and the pipeline-calculated traces.

non-D1 positions, this distance is 300 px); when the background of bright targets are extracted at such close positions of 30 px, some of the astrophysical flux is included as

background and is subtracted from the final spectra, resulting in systematically lower fluxes for D1 spectra of bright targets. This unwanted behavior does not occur when we omit the background removal, which we expect to be low in the D1 positions.

We show the ratios between the newly-extracted spectra using custom traces and the pipeline-extracted spectra in Fig. 6 (the unbinned version of the plot can be found in Fig. 9). For G140L and G140M at CENWAVE 1567 Å, we found that the fluxes with refined empirical traces is mostly within 1% of the fluxes in pipeline traces; for G140M at 1272 Å, the flux ratios remain within 0.5% all across the wavelength range accessible in this configuration.

In the following section, we analyze the fluxes extracted with the custom traces, since they were measured directly in the data instead of relying on the interpolated traces calculated by the pipeline (see Section 3.4.24 of the STIS Data Handbook; Sohn et al. 2019). But the conclusions will be the same if they were analyzed with the pipeline traces.

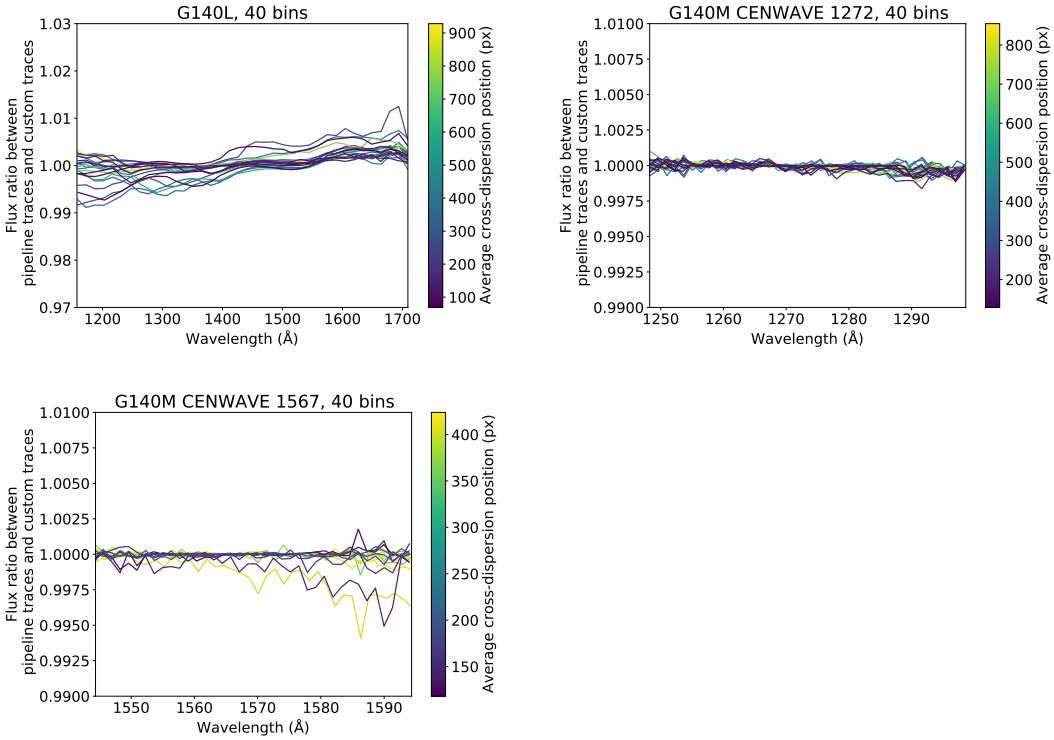

Figure 6. Ratios between the fluxes extracted using the custom traces and the pipeline traces.

3. Results and discussion

To assess the flux repeatability of STIS/FUV-MAMA spectra as a function of position on the detector, we calculated the ratios of the extracted spectra obtained in different cross-dispersion offsets in relation to the flux measured at the nominal position. The nominal position is defined as the exposure with `POSTARG2 = 0.0` and `PROPAPER = 52X2`. The exposure `oehp03060` was discarded because the spectral trace landed partially behind the fiducial bar of the FUV-MAMA detector, yielding a significantly lower flux. The resulting cross-dispersion, nominal positions for the G140L and G140M exposures were ~ 364 and ~ 384 px (1-indexed), respectively.

We assume that the detector non-uniformities at the nominal positions are well characterized and that the flat fields in those regions are accurate. The flux ratios in relation to the nominal position are shown in Figs. 7 and 8. We binned these ratios to a total of 40 bins to highlight potentially uncorrected low-frequency trends; we show the unbinned data at the low-resolution 1024-px range in Appendix A (Fig. 10).

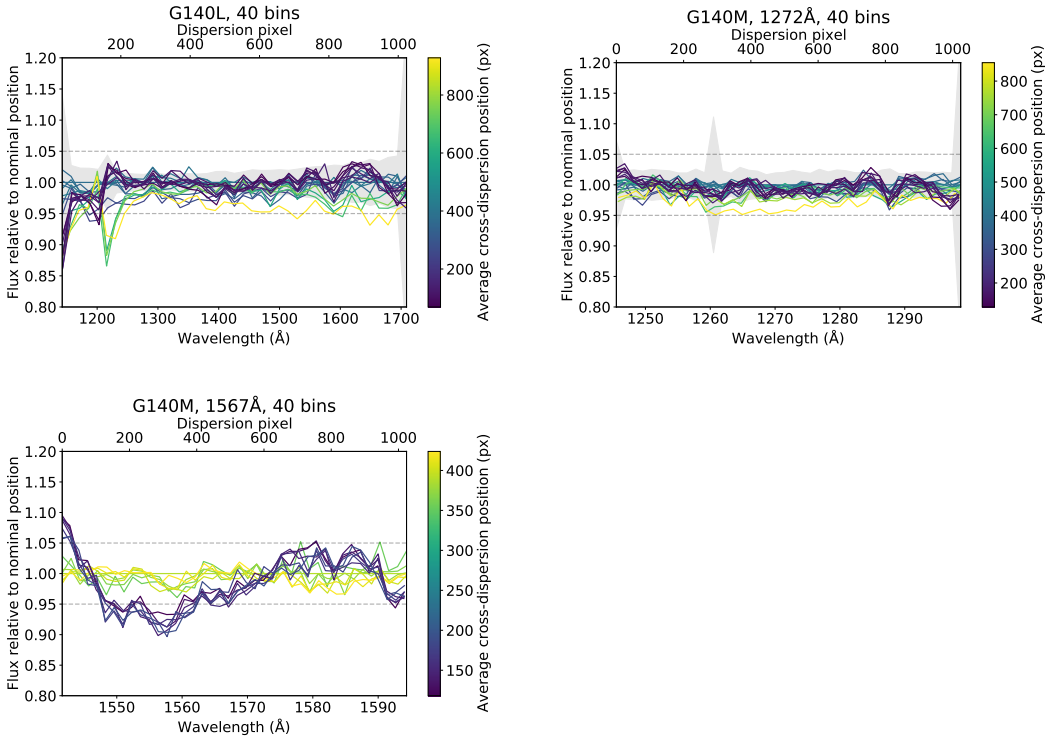

Figure 7. Flux ratios at different cross-dispersion positions in the detector in relation to the nominal position. The shaded regions depicts the standard deviation of non-binned datapoints within each bin. The horizontal dashed lines delimit the 5% flux accuracy.

All but a few exceptions in the ratios we measured are within the accuracy requirement of 5% for STIS/FUV-MAMA all across the detector. For spectra near the

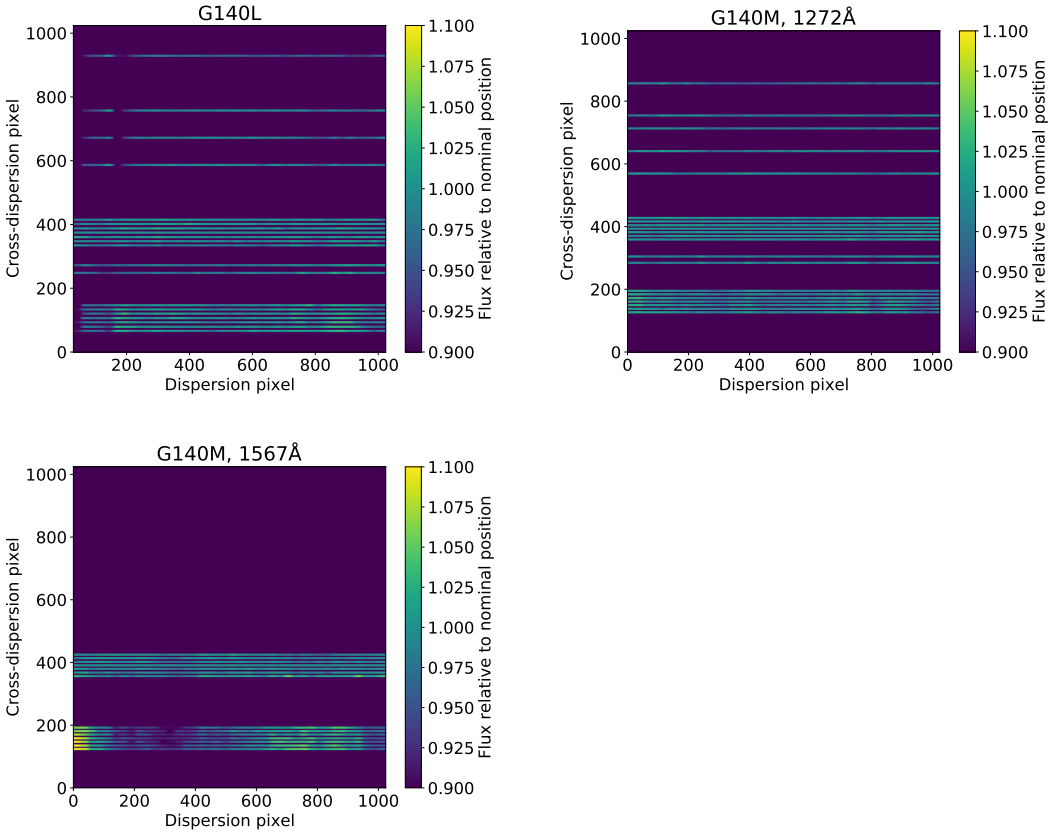

Figure 8. Two-dimensional maps of flux ratios at different cross-dispersion positions in the detector in relation to the nominal position. We note that, for the G140L/1425Å configuration (top left panel), there are no astrophysical fluxes in columns 0 to 31 in low-resolution pixels, so they are omitted from the map.

top of the detector, at cross-dispersion positions $\gtrsim 800$ px (shown as yellow curves in the upper panels of Fig. 7), we find that their ratios deviate the most from the nominal position, but still mostly by a factor within 5% for G140L and G140M/1272Å. Flux ratios at other positions can be systematically lower than the nominal flux by a factor not higher than 2% for cross-dispersion positions that are more than 100 px from the nominal position. The average spread in the flux ratios is on the order of 2%. These variations could explain the spread in TDS residuals seen in Fig. 1, which are also in the order of 2%. Some significant deviations near the Lyman-α line (1215.67 Å) are expected due to the strength of this feature; similarly but to a lesser degree, deviations are also seen near other spectral lines around 1260 Å and 1550 Å. Any mismatches between wavelength solutions of each exposure, even the slightest ones, show up as large differences between exposures taken with the same configuration.

Another systematic effect we identified is the presence of an approximately sinusoidal trend in the flux ratios (Fig. 7) between 200 and 800 low-resolution pixels

with a peak-to-peak amplitude of $\sim$ 4% and a period of $\sim$ 200 px. Particularly, a feature that is consistently seen in the ratios for all configurations (see also the maps in Fig. 8) is the flux drop around 800 px. These effects and the ones described above, although below the 5% flux accuracy requirement, show that there is still room for improvement when it comes to correcting for detector non-uniformities at low frequencies.

More concerning are the lowest positions in the detector (shown with the darkest colors in Fig. 7 for G140M/1567Å, or more precisely those whose cross-dispersion position are $<$ 200 px), since they display the most significant deviations from the nominal flux. These deviations are above the 5% flux accuracy requirement of the FUV-MAMA observations, and are suggestive of uncorrected variations from the dummy flat fielding we had hoped to uncover. However, it is surprising that the other G140M cenwave shows variations well below the 5% threshold. We do note that the signal-to-noise ratio of the G140M/1567Å exposures is approximately half of the G140L and G140M/1272Å exposures, whose deviations are below the 5% limit. Besides the traces, we also investigated the possibility of this effect being caused by the lack of background subtraction in the D1 positions. However, we verified that the detector background contributes to only 0.02% of the observed flux of the star, and cannot be the sole source of the deviations seen in the D1 positions of G140M/1567Å.

4. Recommendations

Our findings suggest that the FUV-MAMA detector uniformities are well characterized for positions near the nominal one ($\sim$ 370 px in the cross-dispersion direction). For G140L and G140M/1272Å, the flux ratios in relation to nominal are within the 5% flux accuracy requirement of STIS, and the same is valid for the D1 positions. However, our analysis suggests there is still room for improvement to correct for systematic effects due to detector non-uniformities at low frequencies. We recommend that, at this moment, efforts in producing L-flats are not strictly necessary to attain the accuracy requirement of STIS/FUV-MAMA observations for both G140L and G140M, but such an effort could be used to correct for the sinusoidal trends seen in Fig. 7.

For D1 positions with the configuration G140M/1567Å in particular, where the exposures had lower SNR, we do find wavelength-dependent deviations above 5% in relation to the nominal position, and we could not identify the source of this deviation. We have ruled out the most likely sources of such errors, namely sub-optimal spectral tracing and background subtraction. In order to investigate the source of these deviations, we recommend further observations of a standard white dwarf with G140M/1567Å and other different wavelength centers in a future special calibration program.

Other than the science cases requiring extreme control of instrumental systematics, we recommend that it is not necessary to turn off the monthly offset to attain the best flux accuracy for targets observed with STIS/FUV-MAMA, as different

positions in the detector do not show deviations stronger than the accuracy requirement of the detector.

Change History for STIS ISR 2022-06

Version 1: 30 September 2022- Original Document

References

Bohlin, R. C., Lindler, D. J. & Baum, S., 1996, STIS Instrument Science Report 1996-15

Bohlin, R. C., Collins, N., Gonnella, A., 1998, STIS Instrument Science Report 1997-14

Carlberg, J., Monroe, T., 2017, STIS Instrument Science Report 2017-06

Dressel, L., Bohlin, R., Lindler, D. & Holfeltz, S., 2007, STIS Instrument Science Report 2007-03

Maclay, M. T., 2021, STIS Instrument Science Report 2021-02

Prichard, L., Welty, D. and Jones, A., et al. 2022 "STIS Instrument Handbook," Version 21.0, (Baltimore: STScI)

Proffitt, C. R., 2006, STIS Instrument Science Report 2006-04

Shaw, D., Kaiser, M. E., & Ferguson, H., 1998, STIS Instrument Science Report 1998-15

Sohn, S. T., et al., 2019, "STIS Data Handbook," Version 7.0, (Baltimore: STScI).

Virtanen, V., Gommers, R., Oliphant, T. E., et al. 2020, "SciPy 1.0: Fundamental Algorithms for Scientific Computing in Python," Nature Methods, 17(3), 261-272.

Appendix A

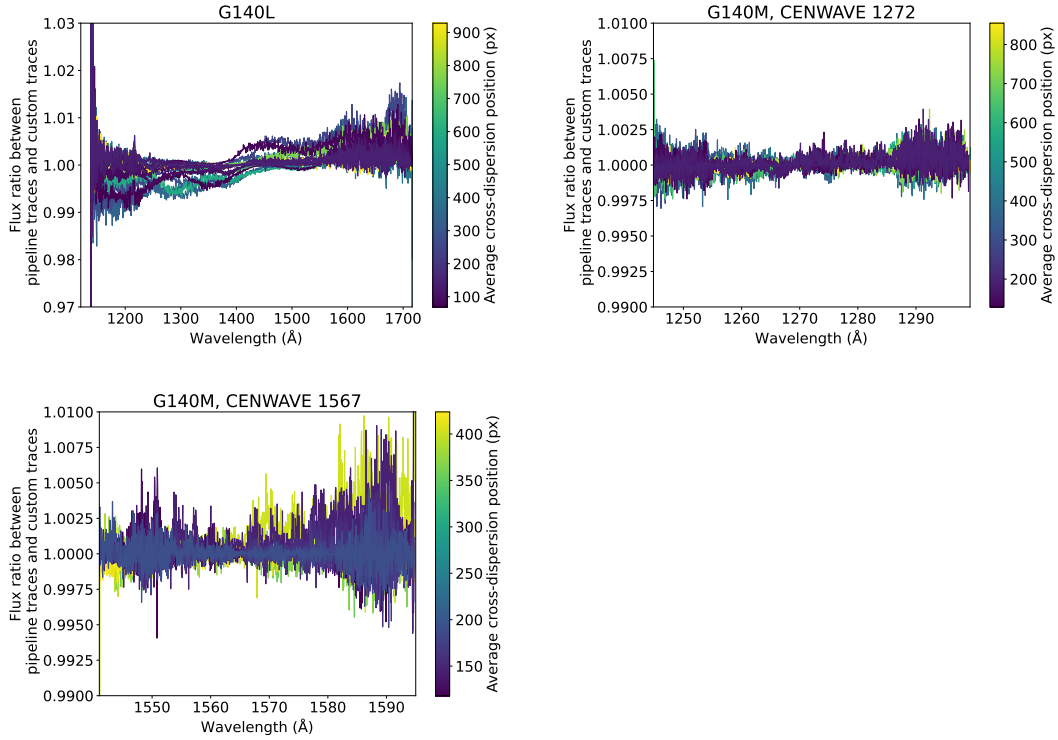

Figure 9. Same as Fig. 6, but the ratios are not binned in wavelength space.

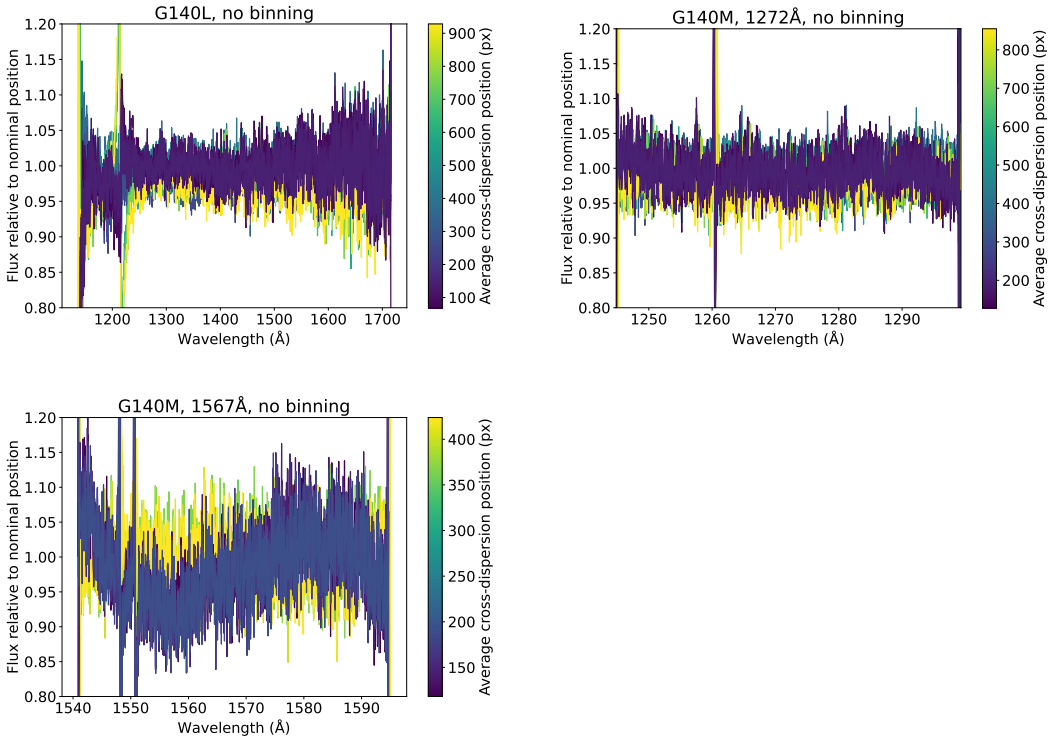

Figure 10. Same as Fig. 7, but the ratios are not binned in wavelength space.